

Magnetic Structure of Bulk GdMnO_3 : Influence of Strain

Hichem Ben Hamed,* Martin Hoffmann, Waheed A. Adeagbo, Arthur Ernst, and Wolfram Hergert

Internal structural distortions are of great interest in the determination of electronic and magnetic properties of the strong correlated rare earth manganites. When combined with external structural modifications like uniaxial or biaxial strains, structural distortions can lead to the emergence of new magnetic ground states. This realization is seemingly more probable with the low-band-width manganite GdMnO_3 on the grounds that it is located in the magneto-electric phase diagram of orthorhombic rare earth manganites between the A-type antiferromagnetic (AFM) order and the cycloidal spin orders. Herein, a thorough analysis of the magnetic structure of GdMnO_3 based on the density functional theory connected with a classical Heisenberg model together with Monte Carlo calculations is presented. It is found whether a compressive uniaxial strain along the c direction or biaxial strain on the ab plane favors a ferromagnetic (FM) ground state over the AFM one. On the contrary, a tensile strain also on the ab plane is likely to stabilize the E-type AFM order.

of their magnetic structures with external stimuli. As examples, we can mention here the application of magnetic^[5] or electric fields,^[6] whereas structural changes might be induced via chemical^[7] or physical means. Substituting the rare earth element by another element, which is known as chemical pressure, can affect the magnetic properties in case of a different valence of the introduced element. A mixed valence state of Mn might cause in addition a strong competition between the superexchange and double exchange mechanisms. On the contrary, the physical means to adjust structural changes, hydrostatic pressure, uniaxial strain, or biaxial strain showing up, e.g., in epitaxial growth, are considerably improved with recent developments in the experimental field.^[8]

1. Introduction

Rare earth manganites RMnO_3 (R = rare earth element) have attracted a lot of interest in recent years due to their intriguing properties. They exhibit rich phase diagrams with spin, charge, and orbital order. Consequently, the RMnO_3 systems show a strong interplay between structural, electronic, and magnetic properties, which give rise to the colossal magnetoresistance effect in manganites.^[1,2]

These materials accommodate in addition different magnetic orders with comparable energies,^[3,4] allowing for an easy control

Being on the borderline between the simple A-type antiferromagnetic order (A-AFM) or other more complicated magnetic structures (see experimental phase diagram in a previous study^[3]), GdMnO_3 will be in the focus of this study. It shows not only a strong magneto-optical coupling,^[9] which makes GdMnO_3 an important candidate for magneto-optical devices, but offers also a rich playground of different magnetic orders to be accessed by external means like structural changes.

As already mentioned, experimental structural changes in GdMnO_3 could be obtained either with a hydrostatic pressure or an epitaxial strain. These two schemes were examined in literature^[8,10–15] and lead to the stabilization of essentially two magnetic orders, namely the ferromagnetic (FM) or E-type AFM (E-AFM) orders (description of these two and more AFM orders is given later).

For instance, the application of a hydrostatic pressure of about 10 GPa using a diamond anvil cell leads to the stabilization of E-type AFM.^[8] The same magnetic order was reported as the ground state of the epitaxial GdMnO_3 films deposited on the (010)-oriented orthorhombic YAlO_3 by means of neutron-diffraction and resonant soft X-ray scattering measurements^[10] and also density functional theory calculations.^[11,12]


In addition, the FM order was found to be stable in GdMnO_3 thin films, prepared by a chemical solution method on oriented Pt substrates.^[13] Even a high Curie temperature of 70 K was reported. A similar finding was also experimentally revealed for the GdMnO_3 thin films grown on the (001) SrTiO_3 substrate,^[14] where the films develop a FM order with a Curie temperature of 105 K. Such order was not only confirmed by density functional calculations for the (001) substrate orientation but also predicted for the (110) direction.^[15]

H. Ben Hamed, Dr. W. A. Adeagbo, Prof. W. Hergert
Institute of Physics

Martin Luther University Halle-Wittenberg
Von-Seckendorff-Platz 1, 06120 Halle, Germany
E-mail: hichem.ben-hamed@physik.uni-halle.de

Dr. M. Hoffmann, Prof. A. Ernst
Institute for Theoretical Physics
Johannes Kepler University Linz
Altenberger Straße 69, 4040 Linz, Austria

Prof. A. Ernst
Max Planck Institute of Microstructure Physics
Weinberg 2, 06120 Halle, Germany

 The ORCID identification number(s) for the author(s) of this article can be found under <https://doi.org/10.1002/pssb.201900632>.

© 2020 The Authors. Published by WILEY-VCH Verlag GmbH & Co. KGaA, Weinheim. This is an open access article under the terms of the Creative Commons Attribution License, which permits use, distribution and reproduction in any medium, provided the original work is properly cited.

DOI: 10.1002/pssb.201900632

Actually, the two aforementioned structural modifications are anisotropic along the three axes,^[10,16] and a straightforward understanding of the mechanisms behind the magnetic phase transitions might be a little bit tricky. To this end, the strain in this study will be restricted to either uniaxial, where just one cell parameter is changed and the two remaining cell parameters were fixed to the equilibrium ones, or an isotropic biaxial strain on the *ab* plane with a relaxation of the out-of-plane cell parameter. The results of the last mentioned strain could serve as a guide for choosing the right substrate to produce a sought magnetic order for GdMnO₃. That means, a certain magnetic order, if obtained by biaxial strain, could be tuned by just looking for a substrate which has a lattice mismatch value corresponding to the strain percentage.

It was shown earlier that the lattice distortions of GdMnO₃ (see **Figure 1**) were the origin of the observed magnetic phase transitions,^[18] mainly due to the strong competition between the different magnetic interactions. In this direction, we aim in this article to understand the underlying magnetic interactions in GdMnO₃ in the absence or the presence of strain with the exchange parameters J_{ij} , which are a measure for the magnetic coupling between a magnetic atom at site *i* and its magnetic neighbors at site *j*. These interactions depend on two main factors: the distance between site *i* and site *j* and as well their atomic environment.

The article is organized as follows. After a summary of the technical considerations including computational details and the equilibrium lattice structure, the theoretical method to calculate the exchange interactions is explained. Next, the magnetic properties of the unstrained structure are discussed together with the effect of each individual lattice distortion on the stability of magnetic orders. Afterwards, both uniaxial and biaxial strain effects on the magnetic structure of GdMnO₃ are investigated. Finally, a conclusion of the obtained results is provided.

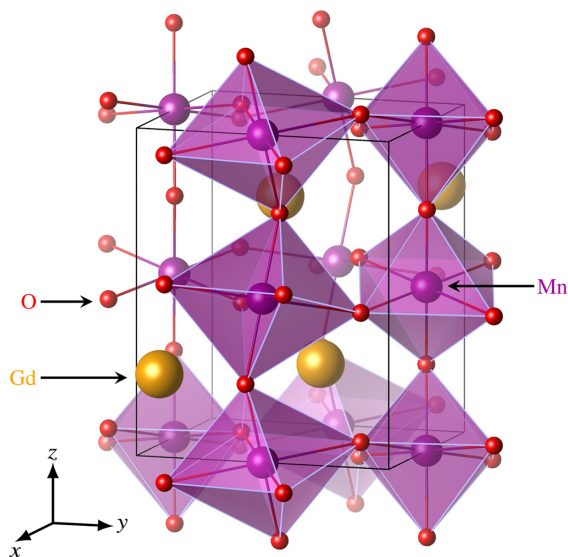


Figure 1. Relaxed structure of orthorhombic GdMnO₃. The internal distortions are visualized by colored polyhedra around the Mn sites formed by the surrounding oxygen atoms. The unit cell has lattice constants *a*, *b*, and *c* along *x*-, *y*-, and *z*-axis, respectively. The underlying structure in this and all following figures were depicted with VESTA.^[17]

2. Computational Details

We applied our multicode approach^[19] based on density functional theory (DFT) calculations with the projector augmented-wave method,^[20,21] as implemented in the Vienna ab initio simulation package (VASP),^[22,23] and the Green's function (GF) method, as implemented in the HUTSEPOT code (the code is available at hutsepot.jku.at).^[19,24] For the treatment of the exchange correlation potential, we used the revised version of Perdew–Burke–Ernzerhof^[25] functional for solids (PBEsol)^[25] in both approaches. In case of VASP calculations, we set the kinetic energy cutoff value for the plane waves to 600 eV and used the Γ -centered $8 \times 8 \times 8$ and $4 \times 4 \times 8$ Monkhorst–Pack *k*-point mesh for the Pbnm unit cell and the supercell, respectively. More details on the calculation cells are given later. We took into account the strong correlation effects by adding an isotropic screened onsite Coulomb interaction^[26] with $U_{Mn} = 2$ eV applied to the Mn 3d whereas the Gd *f* electrons were treated as frozen in the core region. The choice of the *U* value was based on the best compromise in comparison with the experiment between the stability of the magnetic ground state, magnetic moment, and the electronic band gap of the system. More information is given in the Supporting Information of our earlier paper.^[27]

For the GF method calculations,^[19] the potentials of the valence electrons were approximated by the atomic sphere approximation, whereas the cutoff for the spherical harmonics was set to $l_{max} = 3$. We took also correlation corrections into account using the Hubbard-*U* value of 3 eV for Gd and 1 eV for Mn. The choice of Hubbard-*U* value in the GF method is decided foremost on the best match of the obtained density of states from the GF method to the one from VASP calculations. In addition, the magnetic transition temperature calculated by the random phase approximation (RPA) is minimized to agree as much as possible with the experimental magnetic transition temperature of $T_m = 42$ K.^[28] Based on these two criteria, we set $U_{Gd} = 3$ eV and $U_{Mn} = 1$ eV, which gives an RPA $T_m = 48.6$ K, for the subsequent calculations.

To determine more precisely than the RPA method, the magnetic transition temperatures T_m from our calculated Mn–Mn exchange interactions, we used a Monte Carlo method.^[19] Therefore, a cluster consisting of $12 \times 12 \times 12$ times the GdMnO₃ supercell (see **Figure 2**) was constructed from the Mn sublattice alone and periodic boundary conditions were used as well. We assumed first that the thermal equilibrium is reached after 60 000 MC steps. Afterwards, we used also 60 000 MC steps in thermal averaging. We started from a high temperature of 1000 K and cooled down gradually the samples with steps of 3 K. The T_m was then derived from the peak in the heat capacity, whereas its convergence was checked against the number of Monte Carlo steps (one sweep over all sites in the cluster) and the size of the cluster.

2.1. Equilibrium Structure

First, we reconsidered the equilibrium cell parameters of bulk GdMnO₃. Instead of the experimental lattice constants used earlier,^[27] we required the theoretical structural and magnetic ground state as the basis for strain calculations. Therefore, we

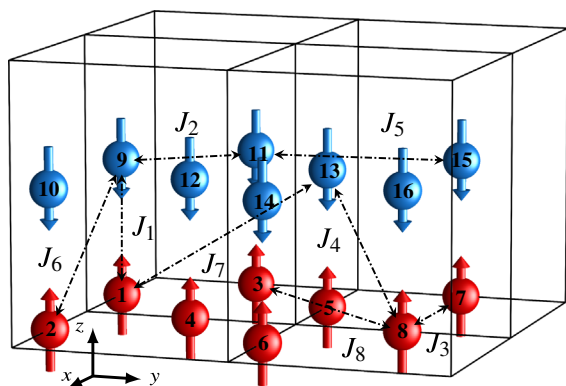


Figure 2. Sketch of the eight exchange interactions between Mn atoms in a supercell of $2 \times 2 \times 1$ of GdMnO_3 used in the Heisenberg Hamiltonian (1) with Mn–Mn distances given in Table 2. For the sake of simplicity, only nonequivalent Mn ions are presented, Gd and oxygen ions are also ignored. The ground-state A-AFM order is shown here with red (blue) balls with arrows for spin up (spin down).

took different Pbnm cell volumes (with 20 atoms) ranging between $\pm 5\%$ of the experimental one and optimized the cell parameters and internal coordinates within each volume with VASP, imposing the A-AFM magnetic ground-state order. By means of this, we obtained the optimal three cell parameters for each of the chosen volumes. Consequently, the resulting total energies of the different volumes were then fitted to $E(V)$ with the Murnaghan equation of state. The volume of the lowest energy from the fitting is again relaxed to obtain its best cell parameters and atomic positions, which converge the interatomic forces below a threshold value of $5 \text{ meV } \text{\AA}^{-1}$. The obtained equilibrium cell parameters and their corresponding bulk modulus B_0 are shown in Table 1 and are compared with other theoretical and experimental results.

The relaxed volume was by 2% smaller than the experimental values.^[29,31] This underestimation of the theoretical equilibrium volume agrees with the observation of a study of Fedorova,^[11] although our approach by starting the relaxations from fixed volumes and the choice of the onsite Coulomb interaction on Mn seems to perform slightly better. The other equilibrium properties, namely the bulk modulus and its derivative, are close to the experimental values.

Table 1. The obtained equilibrium structure of orthorhombic GdMnO_3 calculated with VASP and $U_{\text{Mn}} = 2 \text{ meV}$ compared with another theoretical work^[11] and experimental results.^[29,30]

	a [Å]	b [Å]	c [Å]	V_0 [Å ³]
This work	5.280	5.831	7.364	226.72
Theory ^[11]	5.261	5.807	7.367	225.07
Experiment ^[29]	5.317	5.866	7.431	231.77
	B_0 [GPa]		B'_0	
This work	165.964		4.47	
Experiment ^[30]	170 ± 1		3.72 ± 0.07	

2.2. Heisenberg Model

To improve the description of magnetic properties in RMnO_3 systems in general, we take up again our earlier concept^[27] but increase the number of magnetic exchange interactions J_{ij} between sites i and j considered in the Heisenberg Hamiltonian

$$H = -\frac{1}{2} \sum_{i \neq j} J_{ij} \mathbf{S}_i \cdot \mathbf{S}_j \quad (1)$$

The summation in Equation (1) runs over all sites i , which interact with sites j through the magnetic exchange interactions J_{ij} . The spin moment S in Equation (1) equals to 2 as Mn has 4 unpaired d electrons in GdMnO_3 . A positive (negative) value of the J_{ij} means that the interaction is FM (AFM) between the two sites.

We aim to include the magnetic coupling up to eight magnetic interactions (see Figure 2 and Table 2). That means that we have to consider interactions not only in a single unit cell but use a supercell of $2 \times 2 \times 1$, the orthorhombic Pbnm unit cell, in total 80 atoms. As a result, several different exchange interactions have to play together simultaneously to create a strong and robust FM or AFM order, much more complicated than the simple model with only three interactions.^[27]

Note that we used J_8 with a distance of 7.86 \AA , which is actually not the eighth neighbor but the ninth, as a simplification of the model. The eighth neighbor interaction with a distance of $\approx 7.36 \text{ \AA}$ makes it necessary to use an even larger $2 \times 2 \times 2$ supercell, which would increase the numerical effort too much. Therefore, it was neglected in the model, which is in good agreement with our results from the GF method, where the interaction with $d = 7.36 \text{ \AA}$ remains rather small (see Section 3.1).

To evaluate the aforementioned interactions, we used two different approaches considering the advantages of the two first-principle methods:^[19] 1) total energy mapping with the plane-wave pseudopotential method and 2) the magnetic force theorem within the GF method.

2.3. Energy Difference Method

In the same way as described in a previous study,^[27] we determined the total energies for different magnetic configurations, wrote down an equation for each of them according to Equation (1), and conducted a least square fit for the parameters J_{ij} . Therefore, we need at least eight magnetic configurations, but to improve the fitting procedure, we took into account 14: 12 AFM configurations shown in Figure 3 plus the FM and ferrimagnetic (FiM) states (not shown). The FiM order here is a magnetic order with a net magnetic moment of the cell but smaller than that of the FM order.

Table 2. Distances between Mn atoms of the eight used exchange interactions, given in Å. A sketch of these interactions is shown in Figure 2. The interaction with $d \approx 7.36 \text{ \AA}$ is neglected (see text).

J	1	2	3	4	5	6	7	8
d	3.68	3.93	5.27	5.38	5.83	6.43	6.89	7.86

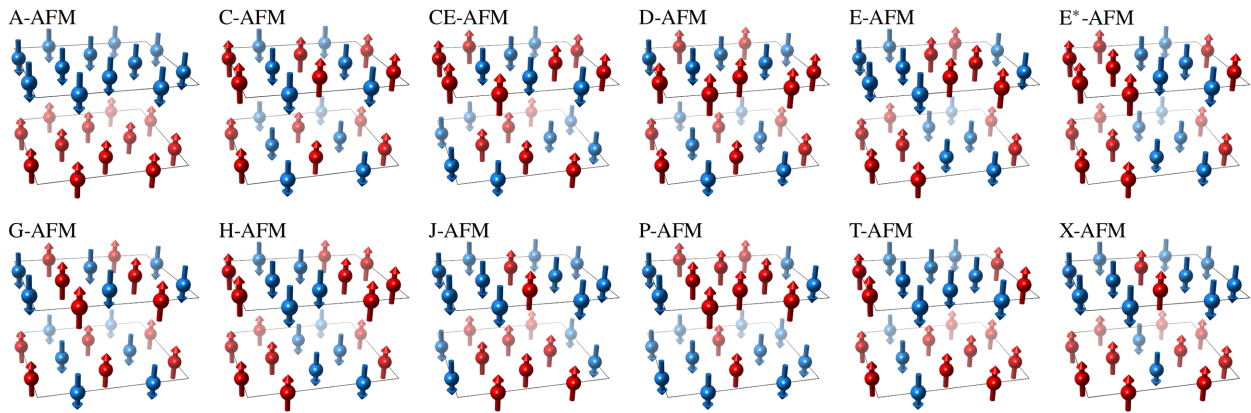


Figure 3. Sketch of the considered AFM structures. Only the magnetic Mn atoms are shown [balls with arrows, red (blue) for spin up (spin down)]. All configurations are represented in a supercell of $2 \times 2 \times 1$ times the orthorhombic unit cell with Pbnm symmetry. We have to note that each supercell contains 16 Mn sites. Each of the AFM structures is explicitly shown in Table 3 by the spin orientation for all asymmetric Mn ions shown in Figure 2.

Table 3. The spin orientation of each of the Mn ions in a supercell of $2 \times 2 \times 1$ of GdMnO₃ shown in Figure 2 with the corresponding magnetic orders shown in Figure 3. The fractional crystal coordinates of all Mn ions inside the same supercell are given as well.

Ion	Coordinates			Magnetic orders											
	x	y	z	A	C	CE	D	E	E*	G	H	J	P	T	X
1	1/4	0	0	↑	↑	↑	↑	↑	↑	↑	↑	↑	↑	↑	↑
2	3/4	0	0	↑	↑	↑	↑	↑	↑	↑	↑	↑	↑	↑	↑
3	0	1/4	0	↑	↓	↑	↓	↑	↑	↓	↑	↓	↑	↓	↑
4	1/2	1/4	0	↑	↓	↓	↓	↑	↑	↓	↑	↓	↑	↓	↑
5	1/4	1/2	0	↑	↑	↓	↑	↓	↓	↑	↓	↓	↓	↑	↓
6	3/4	1/2	0	↑	↑	↓	↑	↓	↓	↑	↓	↓	↓	↑	↓
7	0	3/4	0	↑	↓	↓	↓	↓	↓	↓	↓	↓	↑	↑	↑
8	1/2	3/4	0	↑	↓	↑	↓	↓	↓	↓	↓	↓	↑	↑	↑
9	1/4	0	1/2	↓	↑	↓	↓	↓	↑	↓	↑	↑	↑	↑	↓
10	3/4	0	1/2	↓	↑	↓	↑	↓	↑	↓	↑	↑	↑	↑	↓
11	0	1/4	1/2	↓	↓	↓	↑	↓	↑	↑	↓	↑	↓	↓	↓
12	1/2	1/4	1/2	↓	↓	↑	↓	↓	↑	↑	↓	↑	↓	↓	↓
13	1/4	1/2	1/2	↓	↑	↑	↓	↑	↓	↓	↓	↓	↓	↓	↑
14	3/4	1/2	1/2	↓	↑	↑	↑	↑	↓	↓	↓	↓	↓	↓	↑
15	0	3/4	1/2	↓	↓	↑	↑	↑	↓	↑	↑	↑	↓	↓	↓
16	1/2	3/4	1/2	↓	↓	↓	↓	↑	↓	↑	↑	↑	↓	↓	↓

We note that the lattice structure for the total energy calculations was kept fixed to the ground-state A-AFM structure to have the same Mn–Mn distances and be able to apply Equation (1) consistently. All calculations were done in the $2 \times 2 \times 1$ supercell to avoid problems in the comparison of the total energies. However, not all AFM structures need a supercell setup. For example, the three basic structures (A,C,G) could be obtained only within the unit cell. The spin directions of each Mn ion in these three structures along with other AFM structures are shown in Figure 3 and Table 3.

The total energy of the FiM state E_{FiM} is taken as a reference for the energies to form the 13 considered energy difference

values (index represents the magnetic configuration type, see Figure 3): $E_A, E_C, E_G, E_{\text{FM}}, E_E, E_{E^*}, E_H, E_D, E_{\text{CE}}, E_J, E_P, E_T,$ and E_X , where E_{FM} stands for the total energy of the FM order. Each total energy can be expressed in terms of the eight magnetic exchange interactions J_1, \dots, J_8 by counting the respective number of nearest neighbors, next nearest neighbors, etc.

The whole system of equations resulting from Equation (1) can be expressed finally as a matrix problem by writing down the total energies (same order as earlier) as a vector

$$\mathbf{E} = (E_A, E_C, \dots, E_T, E_X)^T \quad (2)$$

The vector of magnetic exchange interactions is defined as

$$\mathbf{J} = (J_1, \dots, J_8)^T \quad (3)$$

Then, the matrix form of the system of equations to calculate all J_{ij} in the model is given by

$$E = -\frac{S^2}{2} (16\mathbf{T})\mathbf{J} \quad (4)$$

where the matrix \mathbf{T} contains the essential number of interacting Mn atoms and reads (right column only for an overview)

$$\mathbf{T} = \begin{pmatrix} -2 & -4 & 2 & -8 & 2 & -4 & -4 & -4 \\ 2 & -4 & 2 & -8 & 2 & 4 & 4 & 4 \\ -2 & -4 & 2 & 8 & 2 & -4 & -4 & -4 \\ 2 & 4 & 2 & 8 & 2 & 4 & 4 & 4 \\ -2 & 0 & 2 & 0 & -2 & -4 & 4 & -4 \\ 2 & 0 & 2 & 0 & -2 & 4 & -4 & -4 \\ 0 & 0 & 2 & 0 & -2 & 0 & 0 & -4 \\ 0 & -2 & 0 & 0 & 2 & 0 & 0 & 0 \\ -2 & 0 & 0 & 0 & -2 & 0 & 4 & 0 \\ 0 & 0 & 2 & 0 & 0 & 0 & -4 & 0 \\ 0 & 0 & 2 & 0 & 0 & 0 & -4 & 0 \\ 0 & 0 & 2 & -4 & 0 & 0 & 0 & 0 \\ -2 & 0 & 2 & 0 & 0 & -4 & 0 & 0 \end{pmatrix} \begin{matrix} \text{A} \\ \text{E} \\ \text{G} \\ \text{FM} \\ \text{E} \\ \text{E}^* \\ \text{H} \\ \text{D} \\ \text{CE} \\ \text{J} \\ \text{P} \\ \text{T} \\ \text{X} \end{matrix}$$

The resulting J_{ij} are practically averaged for only a specific distance d . Different local structures like variations in the distance to Gd or oxygen between Mn sites with same d are only implicitly included.

2.4. Magnetic Force Theorem

Another approach toward magnetic exchange interactions was developed by Liechtenstein et al.^[32] based on the magnetic force theorem. It determines the exchange interactions with a perturbative approach using the multiple scattering theory within Green's function formalism and is also a fundamental part of our multi-code approach.^[19] The combination of several numerical methods is necessary because structural relaxations are not easily obtained in the GF method. Therefore, we adapt for our GF calculations the same lattice structure as obtained with VASP in the A-AFM magnetic structure as reference and compare the magnetic exchange interactions obtained in both frameworks.

3. Results and Discussion

3.1. Unstrained GdMnO₃

First, we calculated with the magnetic force theorem directly all possible exchange interactions between Mn–Mn, Gd–Mn, and Gd–Gd (Figure 4). We use the same notation for the J_{ij} as proposed earlier in Figure 2. The J_{ij} values within a distance of ≈ 5.36 Å are all within one unit cell. Those reflect our earlier model of three exchange parameters.^[27] Nevertheless, not all of the J_{ij} outside the unit cell can be neglected because they are of the same order of magnitude as those inside, e.g., for the Mn–Mn magnetic coupling constants J_4 , J_5 , or J_8 . In addition, few J_{ij} have different values for the same distance,

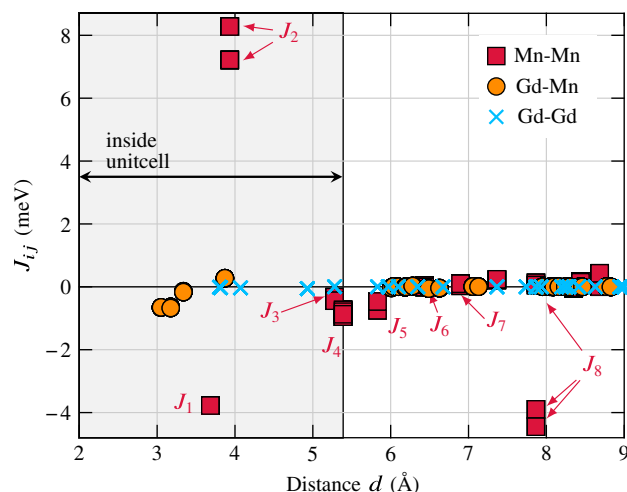


Figure 4. Magnetic exchange interactions of GdMnO₃ calculated with the GF method in dependence on the distances. J_{ij} inside one unit cell are underlaid with gray. Labels J_1, \dots, J_8 represent the respective J_{ij} used in the energy difference method. The Mn–Mn interaction with $d = 7.36$ Å was neglected (not marked, see text). Note that few values are different for the same distance (see text).

e.g., J_8 (Figure 4), in contrast to the distance averaged values of the energy difference method. This stems from small structural variations of the orthorhombic symmetry, which can be only reflected in the results of the GF method. In the latter, the magnetic coupling parameters are determined for each pair of atoms and different angles and distances to oxygen on Gd sites can increase or lower the strength of the coupling even with the same distances between the atoms considered.

We observe the smallest values for Gd–Gd, i.e. 4f–4f, magnetic interactions: $|J_{ij}| \leq 0.1$ meV (see Figure 4). Their negative signs approve an AFM coupling between Gd sites in agreement with the experiment.^[33] Those values explain also the small experimentally obtained magnetic transition temperature of the Gd sublattice of about 7 K. This low T_m is in fact not an exception for Gd but holds true for all rare earth elements in manganites. Therefore, this coupling can be safely neglected in further model Hamiltonians, aiming to study the magnetic properties of RMnO₃.

The more interesting interactions are those between Mn–Mn. In literature, the Mn–Mn interactions are widely discussed for two reasons. The upper part of the valence band is attributed mainly to the Mn e_g states. Therefore, they are mainly involved in the binding, hybridization and exchange, which motivated a lot of studies to restrict the construction of Hamiltonians to those states only.^[34] The coupling between the Mn sites is on the other side rather strong. It reaches a value of about 8 meV for the second-nearest neighbor exchange J_2 (Figure 4). Beyond that, the coupling constants become much smaller. Only J_8 at $d = 7.86$ Å stands out. From the four Mn–Mn exchange interactions with this distance, two of them are smaller than -3 meV and strongly AFM. Therefore, we included this distance also in our energy difference method.

Finally, we studied also the Gd–Mn magnetic coupling parameters. The Gd spins couple only weakly antiferromagnetically to the Mn spins as reported by Hemberger et al.,^[33] with the first

two Gd–Mn exchange interactions being negative by ≈ -0.7 meV and other interaction constants with a larger distance become rather small (see Figure 4). As a consequence, we neglect those interactions later.

By virtue of the observed strengths of the exchange interactions, we extend here our previous study^[27] by considering magnetic interactions up to 7.86 Å in the earlier described energy difference method. The obtained magnetic exchange interactions agree qualitatively very well in the sense of the sign with the aforementioned GF results (see right column in Table 4). Although the nearest neighbor Mn sites (J_1 and J_2) have the strongest magnetic coupling, interactions with further-away Mn sites are still large and might compete for the macroscopic magnetic order.

Apart from the determination of the J_{ij} parameters, we can compare the total energies also directly. The A-AFM configuration of the Mn atoms has, as expected from experimental observations, the lowest total energy for relaxed GdMnO₃ and represents therefore its magnetic ground-state structure (Figure 2). Nevertheless, the energy differences to other magnetic structures are rather small. The total energies of the FM, E-AFM, and H-AFM configurations are about 5 meV per functional unit (f.u.) higher than the one of the A-AFM structure (see energy differences of orthorhombic structure in Figure 5 right panel). This strong competition between different magnetic orders shows the importance of GdMnO₃ as a material which could be easily tuned toward other magnetic phases. In the following paragraphs, we will demonstrate the structural mechanism behind such strong competition.

3.2. Effect of Lattice Distortions

Kimura et al.^[28] attributed the destabilization of the A-AFM structure as the ground state for RMnO₃ in favor of the E-AFM order to the tilting of the MnO₆ octahedra, known as GdFeO₃-type distortion, which is very pronounced in GdMnO₃. Thus, we decompose the cell distortions in GdMnO₃ starting from a purely cubic structure, where the cell parameter for its primitive cell was taken

Table 4. The calculated exchange interactions in GdMnO₃ using the total energy difference method with gradual distortions from the perfect cubic to the orthorhombic ground state structure (see text). J_{ij} are given in meV and magnetic transition temperatures in K. The last row denotes the magnetic character of the respective distorted structure observed in the Monte Carlo simulations.

J_{ij}	Cub	Tet	JT (Q2)	JT (Q3)	GFO	Ortho
J_1	15.83	9.21	6.54	-7.23	-0.71	-1.04
J_2	15.83	18.55	15.23	1.77	1.54	1.89
J_3	-0.06	5.24	4.28	0.44	0.24	0.46
J_4	-0.06	-0.88	-0.14	-0.35	-0.07	-0.11
J_5	-0.06	5.24	5.59	0.42	0.32	0.40
J_6	0.26	1.61	-0.28	0.34	0.22	0.39
J_7	0.26	1.61	0.43	-0.04	-0.05	-0.05
J_8	-2.97	-5.71	-5.60	-0.86	-0.52	-0.70
T_m	926	714	504.4	63.9	40.3	41.0
	FM	FM	FM	AFM	AFM	AFM

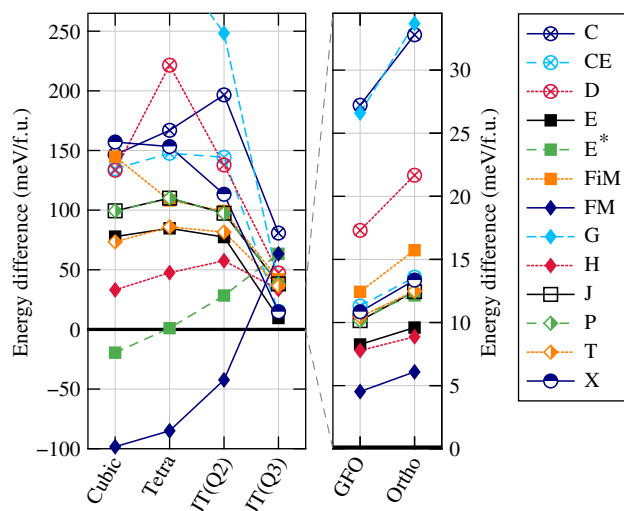


Figure 5. Total energy difference with respect to the final magnetic ground state A-AFM for different magnetic configurations and distortions of the GdMnO₃ lattice. Note that the energy differences for GFO distortion and orthorhombic structure are much smaller than the other distortions (gray dashed lines indicate the different scales).

as $\frac{a}{\sqrt{2}}$ and a is the lattice constant of the relaxed orthorhombic cell along x direction (Figure 1 and Table 4). After that, we took the tetragonal structure keeping the in-plane cell parameter of the primitive cell as before and stretched the out-of-plane cell parameter c to match that of the orthorhombic cell. In both structures, cubic and tetragonal, all atoms remain at their internal high symmetry positions.

Afterwards, the distortion of the MnO₆ cage was gradually introduced, using cell parameters from the orthorhombic structure in three steps. Jahn–Teller distortion Q2 corresponds to two long and four short Mn–O bonds. In the second Jahn–Teller distortion Q3, the MnO₆ octahedron has two long, two medium, and two short Mn–O bonds. The final step before the orthorhombic ground state structure is the cooperative rotation of the MnO₆ polyhedra called GdFeO₃-type (GFO) distortion (Table 4). The Gd ions were kept at the high symmetry points in all gradually distorted structures.

For those structures with the gradual increase of distortions, we calculated again the total energies using the same cell size and number of atoms and all magnetic structures discussed earlier (Figure 5). For the cubic structure, the FM order is most favorable with the E*-AFM order following. Stretching the c parameter in the tetragonal structure slightly reduces the difference between the FM and A-AFM but the E*-AFM order obtains the second lowest energy. All other magnetic structures have a much higher total energy than that of the A-AFM state (Figure 5).

Only taking into account the distortions in the MnO₆ octahedra reduces the total energy difference between the FM and A-AFM states further until A-AFM becomes the ground state for JT(Q3). Most importantly, E-AFM and also the X-AFM energies become very close to the A-AFM energy. This continues to be the case with the inclusion of the octahedra rotations in the GFO structure. Most AFM energies are lowered with this kind of

distortion and come in the range of 10 meV to the A-AFM energy. Including eventually all distortions within the fully relaxed structure of GdMnO₃ does not alter the sequence of the magnetic orders, confirming therewith the earlier hypothesis.^[28]

Further validation of the latter results can be made with the exchange interactions (Table 4). We start from the highest symmetry at the left-hand side of Table 4. Due to the cubic symmetry, the two coupling parameters J_1 and J_2 , the three parameters J_3 , J_4 , and J_5 , as well as J_6 and J_7 are assumed to be equivalent in the fitting procedure of Equation (4). The resulting magnetic ground state is clearly FM, due to the strong FM coupling for the nearest neighbor Mn sites and almost negligible second-nearest neighbor interaction (J_3). Although J_8 has an AFM character (negative), it cannot not overcome ≈ 16 meV for J_1 . This fact can be also observed in the very high magnetic transition temperature of more than 900 K calculated from the magnetic exchange parameters with a Monte Carlo simulation (see Table 4).

Introduction of the tetragonal distortion breaks the symmetry of J_1 and J_2 but the interactions remain FM. Despite the large AFM J_8 , the magnetic ground state still remains FM with a high $T_m = 714$ K because more magnetic exchange parameters show positive contributions, resulting from the straight Mn–O–Mn bonds in this structural setting.

Including also internal structural variations through the Jahn–Teller mode Q2 does not alter the magnetic ground state immediately, which remains FM, but reduces most of the coupling parameters. Only with Q3 distortion and beyond, the ground state starts to be of A-AFM order. This is clearly manifested by the large negative value of J_1 . This fact changes again when the collective rotations of octahedra along c -axis are introduced (GFO distortion). The in-plane bond angle between Mn–O–Mn just changes by 8°, whereas out-of-plane angle is strongly reduced by about 40°. Therefore, the J_1 interaction strength is significantly affected and the A-AFM state is destabilized: The absolute total energy of the A-AFM order for the GFO structure is by ≈ 80 meV f.u.⁻¹ higher than that of the Q3 structure (note that Figure 5 depicts relative energy difference to A-AFM).

Finally, the calculated magnetic transition temperatures show as well the importance of the GFO distortion (Table 4). The

obtained T_m of 40.3 K is very close to that of the orthorhombic symmetry. The latter agrees very well with the measurement of Kimura et al.^[28] Only the Monte Carlo transition temperature of the Q3 structure is still close to the experimental value among the other considered symmetries of GdMnO₃. The remaining structures lead to a high T_m due to the large obtained exchange interactions.

3.3. Strained GdMnO₃

As we discussed in Section 3.1, the considered J_{ij} show different FM and AFM behaviors of comparable strength. This can result in magnetic phase transitions by variations of the magnetic coupling. On the contrary, the latter are strongly affected by internal structural distortions, as demonstrated in Section 3.2, motivating the applications of strain as a tool to tune the magnetic properties of GdMnO₃. We started by checking the effect of uniaxial strain along the three different crystallographic axes on the stability of the magnetic order in GdMnO₃.

3.3.1. Uniaxial Strain

Due to the orthorhombic structure of GdMnO₃ and consequently the challenging numerical task to control the convergence of the two cell parameters if the third one is adjusted, we fixed those along the perpendicular directions of the applied uniaxial strain to their equilibrium values. Therefore the cell volume is adjusted by the same amount of the applied uniaxial strain and the stability of the magnetic orders is checked within the strained volumes.

Being A-AFM for the unstrained system, the magnetic order does not show any transition, whether with compressive or tensile strain up to 3% along the x direction (see Figure 6a). Nevertheless, the energy differences to the E-AFM and H-AFM structures are reduced with a compressive strain. The situation reverses with tensile strain where the total energies of the two previous AFM orders increase, whereas the FM order becomes more favorable. The total energies of the C-AFM and G-AFM configurations remain barely unaffected. For uniaxial strain along the y direction, the order of the total energies of the

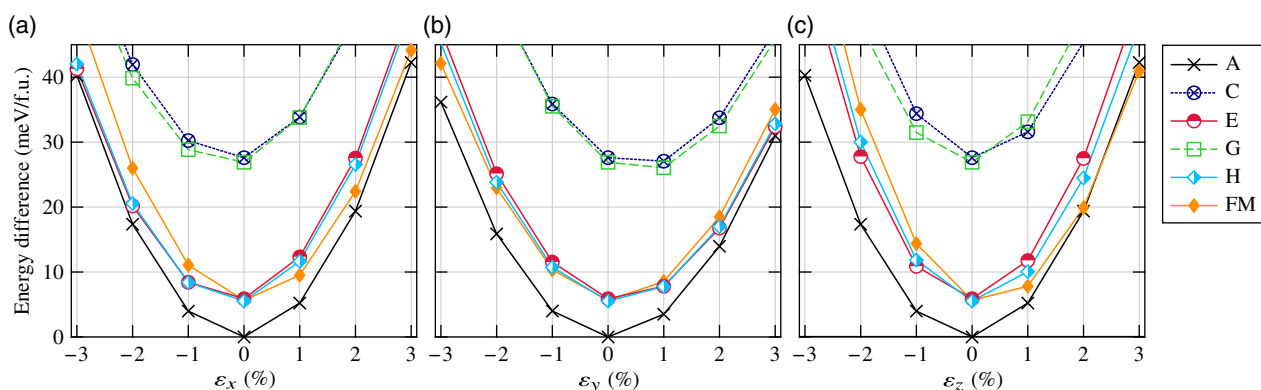


Figure 6. Total energies for the different magnetic configurations for the uniaxial strains in a) x , b) y , c) z directions. At 0% strain, the theoretical lattice structure is used.

magnetic structures does not change notably (see Figure 6b). On the contrary, the situation becomes more interesting for uniaxial strain along the z direction (see Figure 6c). Here, a tensile strain of 3% changes the order of the total energies and the FM order is found to stabilize to the ground state. This amount of strain was insufficient along the other two uniaxial strain directions before. In other words, only a tensile strain in z direction may affect the magnetic ground state of GdMnO_3 . This transition is mainly driven by the drastic change of the calculated value of J_1 . It goes from an AFM coupling of -1.04 meV in the unstrained system to an FM coupling of 0.12 meV. Most of other exchange couplings were slightly affected except the FM J_2 and the AFM J_8 which were strengthened by 0.35 meV and weakened by 0.1 meV, respectively.

3.3.2. Biaxial Strain

We define the biaxial strain as the application of an uniform strain in one plane, here the xy plane. That means that we equally compressed or stretched in our calculations the a and b cell parameters according to the given strain percentage and kept them fixed, whereas the c parameter was relaxed to minimize the total energy (Figure 7).

The application of 1% tensile strain was found to lower the difference between the A-AFM, which still remains the ground state, and the E-AFM state to ≈ 4.5 meV, which was ≈ 5.9 meV before in the unstrained cell. The same holds true for the energy of the H-AFM state, which is now just ≈ 0.8 meV higher than that of the E-AFM state. Increasing the tensile strain further only lowers the energy differences but the A-AFM state remains the magnetic ground state. A similar observation can be made from the magnetic exchange interactions for the tensile strain region (Figure 8a). The variations in J_{ij} are moderate, being in line with the small differences in the energy landscape discussed earlier. Nevertheless, the in-plane magnetic coupling parameters are affected. In particular, J_2 decreases from ≈ 2 meV to almost 1 meV, J_8 from ≈ -0.7 to -0.46 meV, and J_5 from ≈ 0.4 to 0.29 meV. This results in an energetic preference towards E-AFM, which is essentially AFM in the out-of-plane

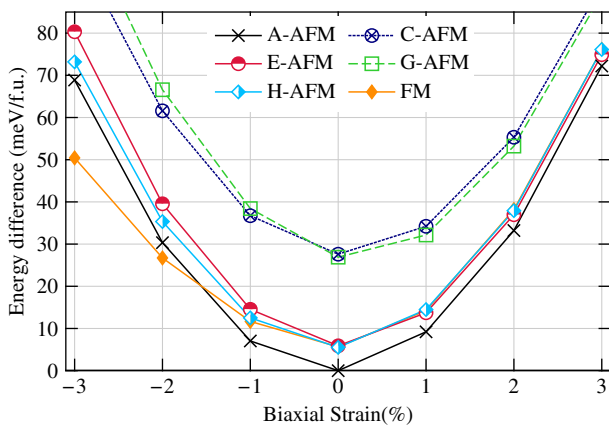


Figure 7. Total energy for the different magnetic configurations for biaxial strains in the xy plane. At 0% strain, the theoretical lattice structure is used.

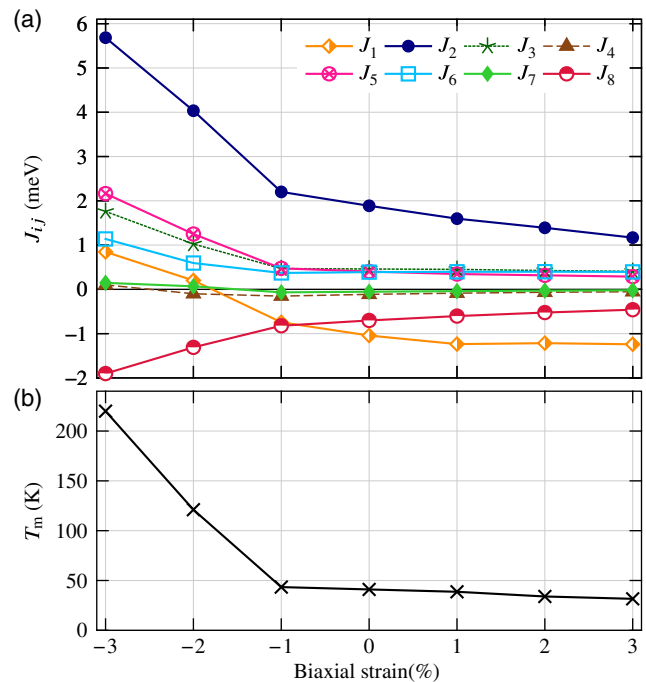


Figure 8. Variation of a) the exchange interactions and b) the magnetic transition temperature T_m in orthorhombic GdMnO_3 with the applied biaxial strain within the xy plane.

direction (negative J_1), similar to A-AFM but has also AFM contributions in a Mn plane (in plane).

On the contrary, compressing the in-plane lattice constants of GdMnO_3 shows a more than a doubling of the value of J_2 (Figure 6a). By the same way, the other FM coupling constants J_3 , J_5 , and J_6 increase their strength with compressive strain. In contrast to the AFM nature of the J_1 , J_4 , and J_7 coupling constants in unstrained GdMnO_3 , the latter develop gradually an FM interaction, which starts at 2% for both J_1 and J_7 and later at 3% strain for J_4 too. Only J_8 remains negative. This goes in line with the total energy difference for compressive strain (Figure 5). At a strain of -2% , the FM order becomes with 3.6 eV more favorable than the A-AFM state.

Those variations of the magnetic interactions are driven by the internal distortions of the MnO_6 octahedra (see Section 3.2). We refer to our previous study^[27] for a thorough discussion of the internal structure of GdMnO_3 . Here, we will only briefly discuss the observed structural variations mainly characterized by the Mn–O bond length and the Mn–O–Mn bonding angles (Table 5). The shortest bond length d_s in the MnO_6 octahedron does not change significantly, but the medium bond length d_m (1.94 Å at zero strain) decreases by 0.2 Å for tensile strains and becomes almost similar to d_s . The latter can hint to a structural transition from JT(Q3) to JT(Q2), which can indicate an FM ground state (Table 4). Surprisingly, d_m increases up to 1.98 Å for compressive strains. Only the longest bond length d_l , in plane and initially 2.21 Å, follows a linear increase from the highest compressive strain of -3% to the highest studied tensile strain of 3% . In addition to the bond lengths, the Mn–O–Mn bond angles indicate as well internal distortions (Table 5). We observe

Table 5. Structural distortion parameters for biaxial strain. The three different Mn–O bond lengths are short (d_s), medium (d_m), and long (d_l) and given in Å. The in-plane and out-of-plane Mn–O–Mn bonding angles are α and β , respectively.^[27]

Strain	d_s	d_m	d_l	α	β
–3%	1.92	1.98	2.06	145.40	148.67
–2%	1.91	1.96	2.12	145.42	146.77
–1%	1.90	1.94	2.16	145.42	145.17
0%	1.91	1.94	2.21	145.50	143.66
1%	1.91	1.92	2.23	145.53	142.14
2%	1.92	1.92	2.27	145.39	140.89
3%	1.92	1.98	2.06	145.40	148.67

no significant change for α in the xy plane varying only in a range of $\pm 0.1^\circ$. However, the out-of-plane bond angle β decreases linearly from 148.67° to 139.85° and, therefore, α becomes larger or smaller than β for compressive or tensile strain, respectively. This indicates again two different kinds of structural distortions for compressive or tensile strain.

The latter increases the GFO structural distortions by decreasing β with more tensile strain (Table 5). Although GFO distortion can contribute to stabilizing the E-AFM magnetic order,^[28] the variation of the out-of-plane Mn–O–Mn bond angle β is not directly reflected in the J_{ij} . Therefore, the stabilization toward the E-AFM magnetic ground state might be driven simultaneously by all variations of the internal distortions (mainly the increase in l and decrease in β).

Finally, we used again the exchange interactions for each biaxial strain value in a Monte Carlo calculation (see Figure 8b). We obtained on the one hand an abrupt increase in the Curie temperature with compressive strain. On the other hand, we observed a minimal decrease in the Néel temperature with tensile strain. The same trend was also reported in the magnetic phase diagram of RMnO_3 ^[28] where the transition temperature decreases linearly from compounds with the A-AFM order to those with E-AFM order. This confirms again a possible magnetic phase transition of GdMnO_3 toward the E-AFM magnetic order with a rather large tensile strain.

4. Conclusion

We discussed extensively the magnetic properties and different magnetic configurations in GdMnO_3 . With our newly proposed extended model, we identified the A-AFM structure as the magnetic ground state of the system by considering not only three nearest-neighbor Mn–Mn exchange interactions but values up to a distance of ≈ 7.86 Å. This distance goes beyond the unit cell of GdMnO_3 and covers also the in-plane interaction J_8 , which was rather large and AFM (negative). It explains the observed close relationship of GdMnO_3 with the H-AFM and E-AFM magnetic orders and the experimental observation of E-AFM under some conditions. Those results were confirmed by magnetic exchange interactions obtained with the magnetic force theorem. However, we have to note that a comparison of our calculated exchange interactions with experimental results is not directly possible

because the latter may include contributions from the magnetism of the rare earth ion, which are up to now not included in our model Hamiltonian.

As main results, we showed how the internal structural distortions play together and contribute to the magnetic ground state as well. All possible lattice distortions of the MnO_6 octahedra had to be taken into account to match the experimentally measured magnetic transition temperature. Starting instead from the fully relaxed structure, we applied uniaxial and biaxial strain to GdMnO_3 . Uniaxial strain did alter the magnetic order only when the cell is compressed along the z direction. However, biaxial strain results in two different behaviors when applied. A compression of the ab plane was able to destroy the AFM coupling in GdMnO_3 and promoted a robust FM order; in addition, tensile strain was able to trigger a phase transition toward the E-AFM. One possible realization of these transitions can be acquired in thin films, where the variation of the substrate can cause epitaxial strain. Also here, a direct comparison between experimental results and calculations with biaxial strain is not straightforward, because the strain could be different in all three dimensions. Nevertheless, our results demonstrate the tailoring of the magnetic properties of GdMnO_3 by small structural distortions, being internally or externally via uniaxial and biaxial strain.

Acknowledgements

This work was funded by the Deutsche Forschungsgemeinschaft (DFG, German Research Foundation), Projektnummer 31047526–SFB 762, project A4 and B1. The computer resources of the Finnish IT Centre for Science (CSC), through Project no. 2000643, are acknowledged. Discussions with P. Paturi and K. Kokko (University of Turku) are gratefully acknowledged.

Conflict of Interest

The authors declare no conflict of interest.

Keywords

density functional theory, GdMnO_3 , Heisenberg model, magnetism

Received: October 1, 2019

Revised: March 4, 2020

Published online: April 8, 2020

- [1] R. von Helmolt, J. Wecker, B. Holzapfel, L. Schultz, K. Samwer, *Phys. Rev. Lett.* **1993**, *71*, 2331.
- [2] M. B. Salamon, M. Jaime, *Rev. Mod. Phys.* **2001**, *73*, 583.
- [3] T. Kimura, G. Lawes, T. Goto, Y. Tokura, A. P. Ramirez, *Phys. Rev. B* **2005**, *71*, 224425.
- [4] Y. Yamasaki, H. Sagayama, N. Abe, T. Arima, K. Sasai, M. Matsuura, K. Hirota, D. Okuyama, Y. Noda, Y. Tokura, *Phys. Rev. Lett.* **2008**, *101*, 097204.
- [5] H. Kuwahara, Y. Tomioka, A. Asamitsu, Y. Moritomo, Y. Tokura, *Science* **1995**, *270*, 961.
- [6] A. Asamitsu, Y. Tomioka, H. Kuwahara, Y. Tokura, *Nature* **1997**, *388*, 50.

- [7] E. O. Wollan, W. C. Koehler, *Phys. Rev.* **1955**, *100*, 545.
- [8] T. Aoyama, A. Iyama, K. Shimizu, T. Kimura, *Phys. Rev. B* **2015**, *91*, 081107.
- [9] A. Pimenov, A. A. Mukhin, V. Y. Ivanov, V. D. Travkin, A. M. Balbashov, A. Loidl, *Nat. Phys.* **2006**, *2*, 97.
- [10] S. Mukherjee, K. Shimamoto, Y. W. Windsor, M. Ramakrishnan, S. Parchenko, U. Staub, L. Chapon, B. Ouladdiaf, M. Medarde, T. Shang, E. A. Müller, M. Kenzelmann, T. Lippert, C. W. Schneider, C. Niedermayer, *Phys. Rev. B* **2018**, *98*, 174416.
- [11] N. S. Fedorova, Y. W. Windsor, C. Findler, M. Ramakrishnan, A. Bortis, L. Rettig, K. Shimamoto, E. M. Bothschafter, M. Porer, V. Esposito, Y. Hu, A. Alberca, T. Lippert, C. W. Schneider, U. Staub, N. A. Spaldin, *Phys. Rev. Mater.* **2018**, *2*, 104414.
- [12] J. T. Zhang, C. Ji, J. L. Wang, W. S. Xia, X. M. Lu, J. S. Zhu, *Phys. Rev. B* **2018**, *97*, 085124.
- [13] Y. Romaguera-Barcelay, J. A. Moreira, A. Almeida, J. Araújo, and J. P. de la Cruz, *Mater. Lett.* **2012**, *70*, 167.
- [14] X. Li, C. Lu, J. Dai, S. Dong, Y. Chen, N. Hu, G. Wu, M. Liu, Z. Yan, J. M. Liu, *Sci. Rep.* **2014**, *4*, 7019.
- [15] J. Zhang, C. Ji, Y. Shangguan, B. Guo, J. Wang, F. Huang, X. Lu, J. Zhu, *Phys. Rev. B* **2018**, *98*, 195133.
- [16] C. Lin, Y. Zhang, J. Liu, X. Li, Y. Li, L. Tang, L. Xiong, *J. Phys.: Condens. Matter* **2012**, *24*, 115402.
- [17] K. Momma, F. Izumi, *J. Appl. Crystallogr.* **2011**, *44*, 1272.
- [18] M. Mochizuki, N. Furukawa, *Phys. Rev. B* **2009**, *80*, 134416.
- [19] M. Hoffmann, A. Ernst, W. Hergert, V. N. Antonov, W. A. Adeagbo, R. M. Geilhufe, H. Ben Hamed, *Phys. Status Solidi B* **2020**, <https://doi.org/10.1002/pssb.201900671>.
- [20] P. E. Blöchl, *Phys. Rev. B* **1994**, *50*, 17953.
- [21] G. Kresse, D. Joubert, *Phys. Rev. B* **1999**, *59*, 1758.
- [22] G. Kresse, J. Furthmüller, *Comput. Mater. Sci.* **1996**, *6*, 15.
- [23] G. Kresse, J. Furthmüller, *Phys. Rev. B* **1996**, *54*, 11169.
- [24] A. Ernst, *Multiple-scattering Theory: New Developments and Applications, Kumulative Habilitationsschrift*, Martin-Luther-Universität Halle-Wittenberg, Halle **2007**.
- [25] J. P. Perdew, K. Burke, M. Ernzerhof, *Phys. Rev. Lett.* **1996**, *77*, 3865.
- [26] S. L. Dudarev, G. A. Botton, S. Y. Savrasov, C. J. Humphreys, A. P. Sutton, *Phys. Rev. B* **1998**, *57*, 1505.
- [27] H. Ben Hamed, M. Hoffmann, W. A. Adeagbo, A. Ernst, W. Hergert, T. Hynninen, K. Kokko, P. Paturi, *Phys. Rev. B* **2019**, *99*, 144428.
- [28] T. Kimura, S. Ishihara, H. Shintani, T. Arima, K. T. Takahashi, K. Ishizaka, Y. Tokura, *Phys. Rev. B* **2003**, *68*, 060403.
- [29] T. Mori, N. Kamegashira, K. Aoki, T. Shishido, T. Fukuda, *Mater. Lett.* **2002**, *54*, 238.
- [30] D. A. Mota, A. Almeida, V. H. Rodrigues, M. M. R. Costa, P. Tavares, P. Bouvier, M. Guennou, J. Kreisel, J. A. Moreira, *Phys. Rev. B* **2014**, *90*, 054104.
- [31] D. V. S. Muthu, A. E. Midgley, P. R. Scott, M. B. Kruger, J. R. Sahu, A. K. Sood, C. N. R. Rao, *J. Phys. Conf. Ser.* **2012**, *377*, 012025.
- [32] A. I. Liechtenstein, M. I. Katsnelson, V. P. Antropov, V. A. Gubanov, V. A. Gubanov, V. A. Gubanov, *J. Magn. Magn. Mater.* **1987**, *67*, 65.
- [33] J. Hemberger, S. Lobina, H. A. Krug von Nidda, N. Tristan, V. Y. Ivanov, A. A. Mukhin, A. M. Balbashov, A. Loidl, *Phys. Rev. B* **2004**, *70*, 024414.
- [34] R. Kováčik, S. S. Murthy, C. E. Quiroga, C. Ederer, C. Franchini, *Phys. Rev. B* **2016**, *93*, 075139.